

Large Area Synthesis of 1D-MoSe₂ Using Molecular Beam Epitaxy

Sock Mui Poh, Sherman J. R. Tan, Xiaoxu Zhao, Zhongxin Chen, Ibrahim Abdelwahab, Deyi Fu, Hai Xu, Yang Bao, Wu Zhou, and Kian Ping Loh*

Transition metal dichalcogenides (TMDCs) belong to a layered class of 2D materials with the general MX₂ (M = Mo, W, etc. and X = S, Se, Te) formula. The confinement of electrons in the 2D limit leads to the emergence of layer-dependent properties due to boundary states and edge polarization effects.^[1] These effects become more pronounced with the dimensional crossover to 1D, where the reduction in dimensionality imposes additional confinement modulation effects, giving rise to novel properties such as 1D confined plasmons,^[2] spin-polarized edge states,^[3] and Tomonaga–Luttinger liquid behavior.^[4] Similar to the layer-dependent tunable properties in 2D-TMDCs, the properties of 1D nanocrystals are expected to be width dependent. It is therefore of great importance to discover a growth method for TMDC nanoribbons which delivers good precision and width control.

Recent advances in top-down TMDC nanoribbon synthesis include focused electron-beam irradiation,^[5] which is able to achieve nanometer precision and control over the wire design. Such a method however suffers from poor scalability. In contrast, bottom-up approaches only manage to obtain wires of the MX type (i.e., Mo₆Se₆, Mo₆S₆, etc.)^[6,7] and it is not until recently that TMDC nanoribbons of the MX₂ type have been synthesized by a template-assisted method.^[8] However, this method requires the use of gold metallic substrate which is not

compatible with device fabrication process. In order to fully tap on the potential of TMDC nanoribbons and integrate them into modern day applications, there is a need to develop a scalable synthesis compatible with current industrial processes.

Herein, we demonstrate the dimensional controlled growth of 2D and 1D-MoSe₂ using molecular beam epitaxy (MBE), where the growth mechanism couples vapor–solid mechanism and van der Waals epitaxy. The resulting nanoribbons are of high quality, as probed by transmission electron microscopy and photoemission spectroscopy. With MBE, the growth is homogeneously distributed with the deposition extent only limited by substrate size and is thus upscalable. The synthesis of such dimensional nanostructures opens up opportunities for the detailed studies of width-dependent, tunable properties. Our growth method is versatile as it can be done on both conducting (highly oriented pyrolytic graphite, HOPG) and insulating (hexagonal boron nitride, hBN) substrates. We further show that the synthesis of 1D-2D hybrid heterostructures can be achieved by adopting a simple two-stage growth process, opening up the possibility of fabricating novel device structures for next-generation device applications.

The synthesis of 2D and 1D-MoSe₂ was carried out using MBE (Figure 1a), where elemental Mo and Se were used as precursors. HOPG was used as the epitaxial substrate, which has the same hexagonal lattice structure as MoSe₂, *D*_{6h} point group, and *P*6₃/*mmc* space group. Our growth method allows us to achieve large area, high density synthesis of 1D-MoSe₂ (Figure 1b). The growth of 2D-MoSe₂ was performed using a substrate temperature of 500 °C (Figure 1c–e) and a high Se:Mo flux ratio consistent with previous growth approaches.^[9,10] As observed in Figure 1c,e, during the initial 2D growth, well-oriented hexagonal domains of MoSe₂ nanoislands are formed, indicating high quality epitaxial synthesis. The domains were characterized by atomic force microscopy (AFM) to have a height of ≈0.8 nm (inset of Figure 1c), which is consistent with monolayer MoSe₂^[11]. Isotropic, lateral epitaxy, aided by the fast diffusion of adatoms to the edges, occurs at 500 °C^[12]. In contrast, fractal growth is obtained at 250 °C due to the lower mobility of adatoms at the edges (Figure S1, Supporting Information). Greater mobility of adatoms at higher temperature allows the growth to be thermodynamically controlled, giving rise to higher crystallinity. With longer growth time, the domain size increases and the isolated crystals coalesce to cover the whole substrate surface (Figure 1d). Second layer growth is also seen, which is evidenced by the height increment of ≈0.8–1.6 nm (inset).

Unexpectedly, when the growth temperature increases to 650 °C while keeping the other growth parameters constant (flux

S. M. Poh, S. J. R. Tan, X. Zhao, Z. Chen,
I. Abdelwahab, Dr. D. Fu, Dr. H. Xu,
Y. Bao, Prof. K. P. Loh
Department of Chemistry
National University of Singapore
Science Drive 3, 117543 Singapore, Singapore
E-mail: chmlhokp@nus.edu.sg



S. M. Poh, S. J. R. Tan, X. Zhao, Z. Chen, I. Abdelwahab
NUS Graduate School for Integrative Sciences and Engineering
Centre for Life Sciences #05-01
28 Medical Drive, 117456 Singapore, Singapore

X. Zhao, Prof. W. Zhou
Materials Science and Technology Division
Oak Ridge National Laboratory
Oak Ridge, TN 37831, USA

Prof. W. Zhou
School of Physical Sciences
CAS Key Laboratory of Vacuum Physics
University of Chinese Academy of Sciences
Beijing 100049, China

Prof. K. P. Loh
SinBeRISE at CREATE
National Research Foundation
CREATE Tower, 1 Create Way, 138602 Singapore, Singapore

DOI: 10.1002/adma.201605641

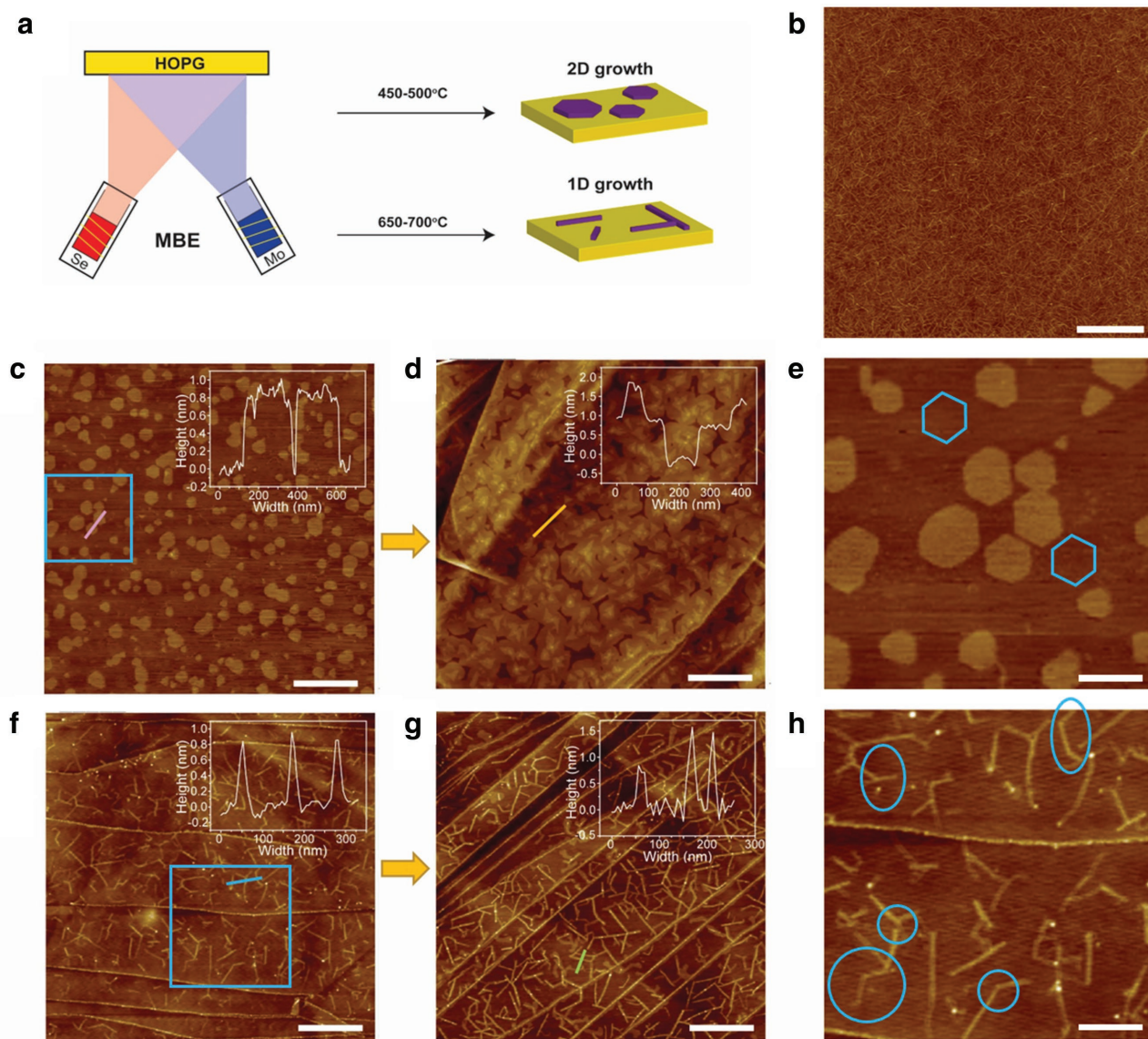


Figure 1. MBE-grown MoSe₂ with 2D and 1D growth modes. a) Schematic illustration of the MBE growth. b) Large-area homogeneous dense growth of 1D-MoSe₂, from 3.5 h growth. c–h) AFM topography images of MoSe₂ synthesized by 2D growth mode for c) 1 h and d) 2 h, and e) the enlarged image of the square in (c); and by 1D growth mode for f) 1 h and g) 2 h, and h) the enlarged image of the square in (f). The insets of (c), (d), (f), and (g) show the height profiles of the color line marked in the image. The hexagons are drawn in (e) to show the orientation of the hexagonal domains. Circled locations in (h) show the regions where there are 60° oriented growth. Scale bar: b) 2 μm, c,d,f,g) 600 nm, e) 150 nm, and h) 220 nm.

ratio and growth duration), drastic changes in the morphology are observed (Figure 1f–h). As shown in Figure 1f, MoSe₂ nanoribbons with an average width of ≈15 nm and aspect ratio ranging from 4 to 30 are observed. The nanoribbons show a loose 60° orientation preference, in which some of the ribbons grow 60° relative to each other (circled in Figure 1h). This suggests a weak epitaxial interaction with the substrate. Furthermore, when the same growth was performed on SiO₂, no 1D growth was observed (Figure S1, Supporting Information). It should be pointed out that such 1D features appear right at the early stage of growth (Figure 1f), and its growth patterns are distinct to that of 2D growth (Figure 1c). The height of these 1D features are ≈0.8 nm (inset of Figure 1f), which corresponds

to monolayer MoSe₂. With longer growth time, the nanoribbon network grows denser with the average width of nanoribbons <30 nm and height increasing to ≈1.5 nm (Figure 1g), which corresponds to the height of bilayer MoSe₂. Importantly, it shows no sign of increase in domain size that would subsequently covers the whole substrate surface. Instead, multilayered networks of 1D-MoSe₂ nanoribbons are obtained (Figure 1b,g). Furthermore, it is noted that the growth occurs on the terraces of the HOPG, and thus is not mediated by the steps. The growth mechanism of such 1D features will be discussed in later section.

In order to investigate the physical and chemical properties of the MBE-grown MoSe₂, we performed Raman spectroscopy

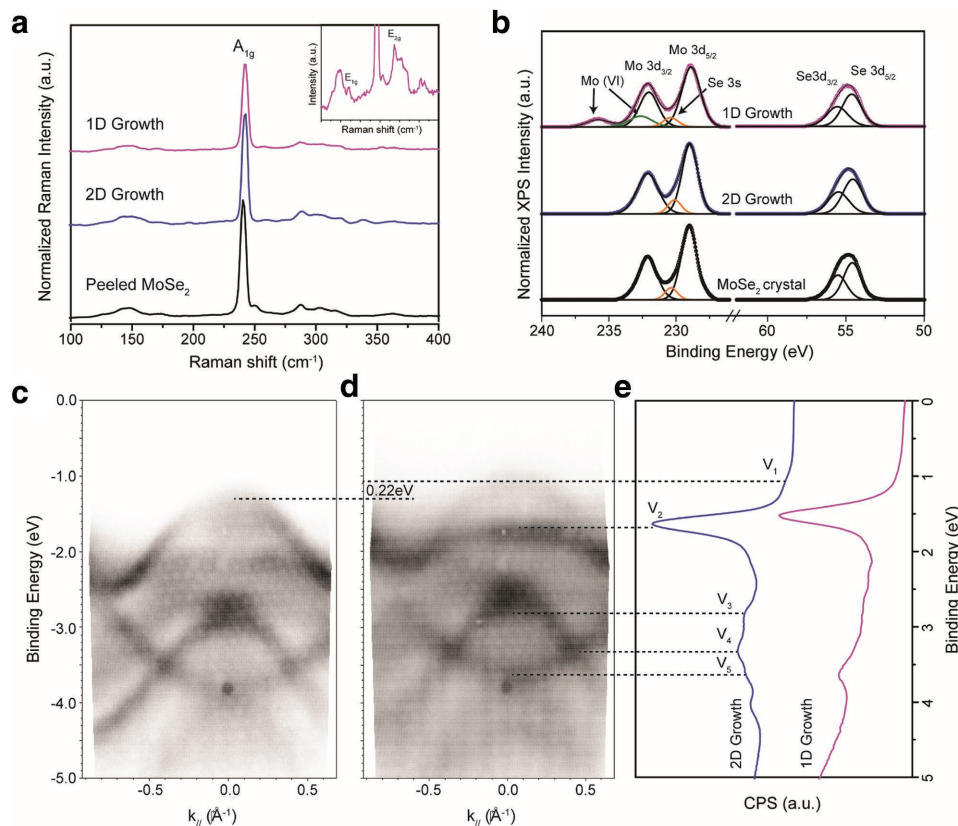


Figure 2. Spectroscopic characterizations of MBE-grown MoSe₂. a) Raman spectra of MoSe₂ synthesized by 1D and 2D growth modes. Raman spectrum of exfoliated (peeled) MoSe₂ is added as a reference. Inset shows the plot at a smaller intensity range to highlight some of the Raman peaks. b) XPS spectra of MoSe₂ synthesized by 1D and 2D growth modes. XPS spectrum of bulk single crystal MoSe₂ is added as a reference. c,d) ARPES spectra showing the electronic band dispersion of c) bulk single crystal MoSe₂ and d) MBE-grown 2D-MoSe₂ on HOPG. e) UPS spectra of MoSe₂ synthesized by 1D and 2D growth modes.

and photoemission spectroscopy. As shown in **Figure 2a**, the Raman peaks at 242, 170, and 287 cm⁻¹ can be assigned to the characteristic out-of-plane A_{1g}, and in-plane E_{1g} and E_{2g} modes of MoSe₂, respectively.^[13] These clearly identify the 1D features grown at 650 °C to be MoSe₂, which are distinct from the MX₂ type nanowires.^[6,7]

X-ray photoemission spectroscopy (XPS) was performed to determine the elemental composition and bonding states of the MBE-grown nanoribbons (**Figure 2b**). The peaks with binding energies of ≈232.1, 228.9, 55.5, and 54.6 eV are assigned to Mo 3d_{3/2}, Mo 3d_{5/2}, Se 3d_{3/2}, and 3d_{5/2} core level orbitals, respectively, which are in good agreement with reported literature values.^[14] The measured Mo 3d and Se 3d core level peaks are similar to that of the bulk single crystal. Moreover, elemental composition analysis performed by integrating the area under the Mo 3d and Se 3d core level peaks indicates the Mo:Se ratio of the nanoribbons to be ≈1:2, which is stoichiometric with MX₂. Additionally, we observed XPS peaks assignable to the Mo (VI) oxidation state in the MoSe₂ nanoribbons, which may originate from the edge atoms.^[8,15] In view of the high density of edge atoms which can have catalytic activities, we tested the hydrogen evolution reaction (HER) on the nanoribbons and 2D-film MoSe₂ samples. The Tafel slope reduces from 213 to 130 mV per decade when MoSe₂ changes from 2D to 1D

(**Figure S2**, Supporting Information). Furthermore, a low onset potential of 56 mV is observed for the MoSe₂ nanoribbons, suggesting their potential as HER catalyst.

In order to investigate the electronic structure of MBE-grown MoSe₂, we performed angle-resolved photoemission spectroscopy (ARPES) and ultraviolet photoemission spectroscopy (UPS). As shown in **Figure 2c,d**, as-grown 2D-MoSe₂ on HOPG has similar band dispersion as bulk MoSe₂ single crystal, further confirming the van der Waals epitaxy and the weak coupling between MBE-grown MoSe₂ and HOPG substrate. The electronic band dispersions are well defined, which is indicative of its high crystal quality (5 mm spot size). Our UPS study shows various valence band peaks for both 1D and 2D grown MoSe₂, labeled as V₁₋₅ (**Figure 2e**). These peaks correspond well to the electronic bands obtained by ARPES (**Figure 2c,d**). V₁ originates from the spin-split band that occurs at the K point while V₂₋₅ originate from dispersive bands predominantly of hybridized Mo-d and Se-p character.^[10] The similarity in the valence band structures of MoSe₂ synthesized by 1D and 2D growth modes indicates their similar chemical composition, despite their morphological differences.

Scanning transmission electron microscopy–annular dark field (STEM-ADF) imaging was further employed to elucidate the atomic structure and grain orientation of the 1D-MoSe₂

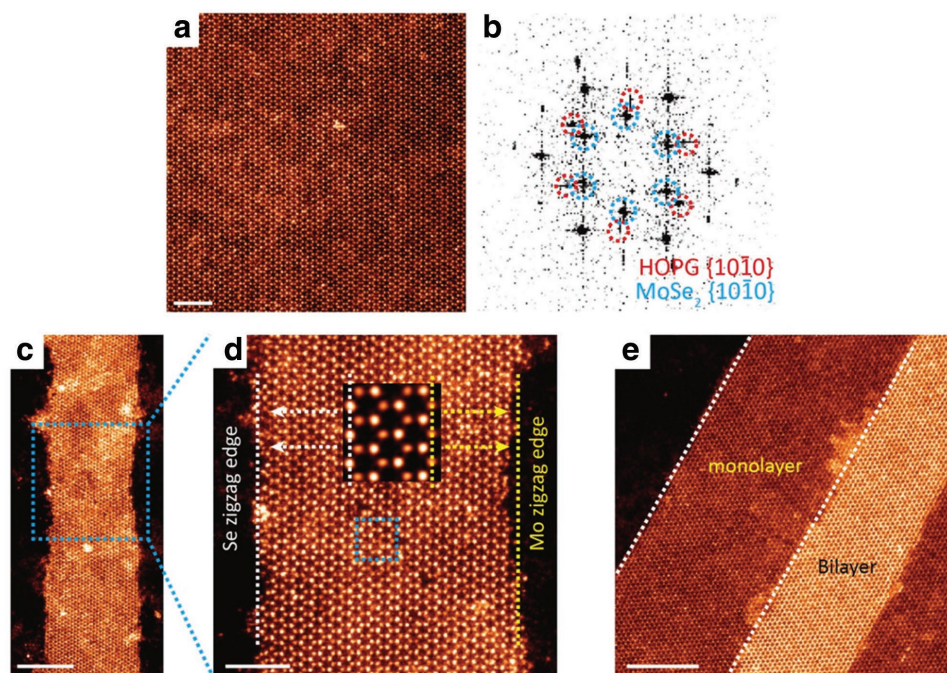


Figure 3. Electron microscopy characterization of 1D-MoSe₂ nanoribbon. a) Atomic resolution STEM-ADF image of monolayer MoSe₂ nanoribbon and b) its corresponding fast Fourier transform (FFT) pattern. c) STEM-ADF image of the MoSe₂ nanoribbon and d) its enlarged image showing alternate Mo- and Se-zigzag edges at two sides. e) STEM-ADF image of a bilayer 1D-MoSe₂ nanoribbon. Scale bar used for (a) and (d) is 2 nm and for (c) and (e) is 5 nm.

(Figure 3). Figure 3a shows the atomically resolved STEM-ADF image of the 1D-MoSe₂ nanoribbon. Long-range periodic bright and dim columns are observed in MoSe₂ honeycomb pattern, which represent the Se₂ and Mo atoms, respectively. Few Se vacancies are seen within the observation area, indicating the high crystallinity of the monolayer 1D-MoSe₂ nanoribbon. Its corresponding fast Fourier transform (FFT) pattern is displayed in Figure 3b. Notably the MoSe₂-HOPG epitaxial relationship is observed, as indicated by the alignment of the (10 $\bar{1}$ 0) crystallographic face of MoSe₂ and HOPG. The lattice constants are measured to be 3.29 and 2.46 Å respectively, which is similar to the bulk lattice constants of each. This shows that there is negligible strain between the van der Waals epitaxially grown layer and the substrate. However, we do note that such epitaxial relationship is not fully adhered to, as there are also regions of nonaligned growth.

Figure 3d shows the edge configurations of the 1D-MoSe₂, with its large-field image in Figure 3c. Intriguingly, it shows that the nanoribbons preferentially grew along the armchair direction with exposed zigzag edges. The two edges are terminated alternatively with Se- and Mo-zigzag edges, which are highlighted in the inset. This observation agrees with previous report that armchair edges are rarely seen due to its high formation energy.^[7] In addition, the STEM-ADF image of a bilayer 1D-MoSe₂ (Figure 3e) shows that the second layer also grows epitaxially along the armchair direction, following the crystallographic orientation of the first layer, with 2H stacking.

Since temperature is one of the key factors (Figure 1) in the selective synthesis of 2D and 1D-MoSe₂, we performed a systematic study of MoSe₂ growth at different temperatures

(Figure 4). For a fair comparison, the growth duration was varied to obtain trilayer height at each growth temperature (≈ 3 nm, with reference to the height scale bar). Figure 4a shows that by changing the growth temperature from 550 to 700 °C, the width of MoSe₂ nanoribbons can be tuned from 80 to 15 nm, with highly uniform coverage (Figure 4b–f). This illustrates the ability of the MBE method to achieve dimensional control of 2D and 1D-MoSe₂ growth.

On closer scrutiny, these temperature-dependent experiments show that the optimum growth temperature for 1D-MoSe₂ occurs at ≈ 650 °C, which has the narrowest width distribution (Figure 4d). Thickness control thus can be further achieved, by controlling the growth duration; on the same note, density control can be achieved by flux rate and growth duration. When temperature is too high, whiskers growth are observed (Figure 4e,f), with nanodots found at the end. These dots are Mo metal nanoparticles that can self-catalyze and mediate the anisotropic 1D growth, as is typical of vapor-phase growth mechanism.^[16] At higher temperature, there is greater desorption of Se and a higher concentration of Mo nanoparticles begin to exert catalytic effect on 1D growth. The adatoms will also enjoy higher mobility and are inclined to grow at the more reactive Mo sites at the tips of the nanoribbons to propagate the 1D growth. This hypothesis is supported by our growth studies using reduced Se precursor flux at the growth temperature of 500 °C, in which a transition from 2D to 1D growth mode can be observed (Figure S3, Supporting Information).

Figure 5 shows that 1D-MoSe₂ ribbon can also be grown on insulating hBN substrate. Similar to the growth on HOPG, 2D layered morphology is obtained at 500 °C growth temperature

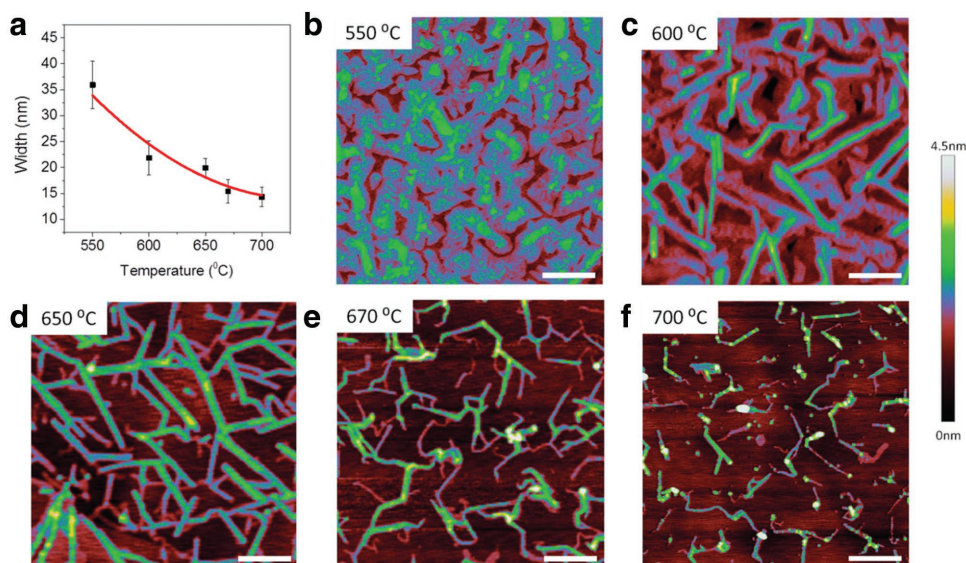


Figure 4. Width control of MBE-grown MoSe₂. a) Scattered plot of width of synthesized MoSe₂ against growth temperatures. Corresponding AFM images of MoSe₂ synthesized at b) 550 °C, c) 600 °C, d) 650 °C, e) 670 °C, and f) 700 °C. Color scale is selected for visual enhancement, normalized across (b)–(f). Scale bar used is 200 nm.

(Figure 5a,d) and 1D nanowires at 650 °C (Figure 5b,e). This demonstrates the versatility of the growth method, being applicable to both insulating and conducting substrates. Furthermore, we also show that 1D-2D hybrid heterostructures can be achieved by adopting a simple two-stage growth using a substrate temperature of 500 °C followed by 650 °C (Figure 5c,f). This opens up the possibility of novel device structures for next-generation device applications.

In conclusion, we report the dimensionally controlled growth of 2D and 1D-MoSe₂ using MBE. The presence of a high density of edge states in these nanoribbons can be exploited in

catalysis, e.g. HER, where superior performance is obtained compared to the 2D films. The MBE growth method, which is scalable on both insulating and conducting substrates, opens up opportunities for large scale integration of 1D-2D hybrid heterostructures for next generation device applications.

Experimental Section

Sample Preparation: MoSe₂ samples were grown in an MBE chamber of base pressure $\approx 6 \times 10^{-10}$ torr. Prior to growth, the substrates were

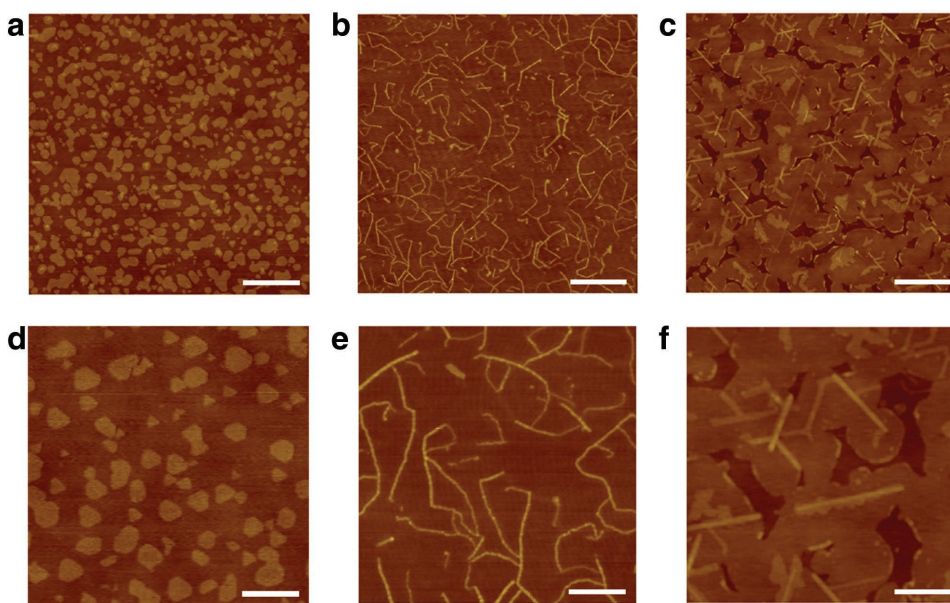


Figure 5. MBE growth of MoSe₂ on hBN. a) 2D growth at 500 °C. b) 1D growth at 650 °C. c) 1D-2D hybrid heterostructures. d–f) The corresponding magnified images of (a)–(c). Scale bar used for (a)–(c) is 600 nm and for (d)–(f) is 200 nm.

degassed in ultra-high vacuum (UHV) chamber for 1 h and annealed at the growth temperature for 10 min. Growth of 2D and 1D-MoSe₂ was carried out at substrate temperature 500 and 650 °C, respectively, unless otherwise stated. Ultrapure Mo and Se were evaporated from an electron beam evaporator and a standard Knudsen cell, respectively. Mo and Se were deposited simultaneously with flux ratio of ≈1:10 for both 2D and 1D-MoSe₂ growth, unless otherwise stated. Growth rate was ≈0.6 ML h⁻¹, at pressure of 1 × 10⁻⁸ torr. No post annealing was done.

Sample Characterization: AFM were performed using a Bruker Dimension FastScan Atomic Force Microscope in tapping mode at room temperature. Raman spectra were recorded at room temperature using the confocal WiTec Alpha 300R Raman Microscope with laser excitation at 532 nm and power of <300 μW. STEM-ADF was performed using an aberration-corrected Nion UltraSTEM-100, equipped with a cold field emission gun, operating at 100 kV. XPS measurements were carried out using SPECS XR-50 X-ray Mg Kα source with the pass energy of 30 eV and spot size of 5 mm. XPS peak fitting was carried out using a mixed Gaussian–Lorentzian function after a Shirley background subtraction. UPS and high-resolution ARPES measurements were carried out with a differentially pumped UVS300 helium discharge lamp (SPECS GmbH) as the light source, which provided monochromatized photon energies of 21.2 eV (He I) and 40.8 eV (He II), respectively, through a toroidal mirror monochromator (SPECS GmbH). XPS, UPS, and ARPES were performed in chamber of base pressure better than 8 × 10⁻¹⁰ mbar.

Supporting Information

Supporting Information is available from the Wiley Online Library or from the author.

Acknowledgements

The authors thank the support of National Research Foundation under its mid-sized Centre program: Centre for Advanced 2D Materials. The electron microscopy work was supported in part by the U.S. Department of Energy, Office of Science, Basic Energy Science, Materials Sciences and Engineering Division (X.Z. and W.Z.), and through a user project at ORNL's Center for Nanophase Materials Sciences (CNMS), which is a DOE Office of Science User Facility.

Received: October 19, 2016

Revised: November 20, 2016

Published online:

- [1] a) K. F. Mak, C. Lee, J. Hone, J. Shan, T. F. Heinz, *Phys. Rev. Lett.* **2010**, *105*, 136805; b) S. Wu, J. S. Ross, G.-B. Liu, G. Aivazian, A. Jones, Z. Fei, W. Zhu, D. Xiao, W. Yao, D. Cobden, X. Xu, *Nat. Phys.* **2013**, *9*, 149; c) Y. Yu, S.-Y. Huang, Y. Li, S. N. Steinmann, W. Yang, L. Cao, *Nano Lett.* **2014**, *14*, 553.
- [2] a) K. Andersen, K. W. Jacobsen, K. S. Thygesen, *Phys. Rev. B* **2014**, *90*, 161410; b) Z. Fei, M. D. Goldflam, J. S. Wu, S. Dai, M. Wagner, A. S. McLeod, M. K. Liu, K. W. Post, S. Zhu, G. C. A. M. Janssen, M. M. Fogler, D. N. Basov, *Nano Lett.* **2015**, *15*, 8271.
- [3] a) Y. Li, Z. Zhou, S. Zhang, Z. Chen, *J. Am. Chem. Soc.* **2008**, *130*, 16739; b) C. Ataca, H. S. ahin, E. Aktürk, S. Ciraci, *J. Phys. Chem. C* **2011**, *115*, 3934; c) M. Gibertini, N. Marzari, *Nano Lett.* **2015**, *15*, 6229.
- [4] H. Ishii, H. Kataura, H. Shiozawa, H. Yoshioka, H. Otsubo, Y. Takayama, T. Miyahara, S. Suzuki, Y. Achiba, M. Nakatake, T. Narimura, M. Higashiguchi, K. Shimada, H. Namatame, M. Taniguchi, *Nature* **2003**, *426*, 540.
- [5] J. Lin, O. Cretu, W. Zhou, K. Suenaga, D. Prasai, K. I. Bolotin, N. T. Cuong, M. Otani, S. Okada, A. R. Lupini, J. C. Idrobo, D. Caudel, A. Burger, N. J. Ghimire, J. Yan, D. G. Mandrus, S. J. Pennycook, S. T. Pantelides, *Nat. Nanotechnol.* **2014**, *9*, 436.
- [6] L. Venkataraman, C. M. Lieber, *Phys. Rev. Lett.* **1999**, *83*, 5334.
- [7] J. Kibsgaard, A. Tuxen, M. Levisen, E. Lægsgaard, S. Gemming, G. Seifert, J. V. Lauritsen, F. Besenbacher, *Nano Lett.* **2008**, *8*, 3928.
- [8] H. Xu, Z. Ding, C. T. Nai, Y. Bao, F. Cheng, S. J. R. Tan, K. P. Loh, *Adv. Funct. Mater.* **2016**, DOI: 10.1002/adfm.201603887.
- [9] A. Roy, H. C. Movva, B. Satpati, K. Kim, R. Dey, A. Rai, T. Pramanik, S. Guchhait, E. Tutuc, S. K. Banerjee, *ACS Appl. Mater. Interfaces* **2016**, *8*, 7396.
- [10] M. M. Ugeda, A. J. Bradley, S. F. Shi, F. H. da Jornada, Y. Zhang, D. Y. Qiu, W. Ruan, S. K. Mo, Z. Hussain, Z. X. Shen, F. Wang, S. G. Louie, M. F. Crommie, *Nat. Mater.* **2014**, *13*, 1091.
- [11] M. M. Benameur, B. Radisavljevic, J. S. Héron, S. Sahoo, H. Berger, A. Kis, *Nanotechnology* **2011**, *22*, 125706.
- [12] H. Roder, E. Hahn, H. Brune, J.-P. Bucher, K. Kern, *Nature* **1993**, *366*, 141.
- [13] a) D. Nam, J. U. Lee, H. Cheong, *Sci. Rep.* **2015**, *5*, 17113; b) P. Tonndorf, R. Schmidt, P. Böttger, X. Zhang, J. Börner, A. Liebig, M. Albrecht, C. Kloc, O. Gordan, D. R. T. Zahn, S. M. de Vasconcellos, R. Bratschitsch, *Opt. Express* **2013**, *21*, 4908.
- [14] X. Wang, Y. Gong, G. Shi, W. L. Chow, K. Keyshar, G. Ye, R. Vajtai, J. Lou, Z. Liu, E. Ringe, B. K. Tay, P. M. Ajayan, *ACS Nano* **2014**, *8*, 5125.
- [15] H. Xu, S. Liu, Z. Ding, S. J. Tan, K. M. Yam, Y. Bao, C. T. Nai, M. F. Ng, J. Lu, C. Zhang, K. P. Loh, *Nat. Commun.* **2016**, *7*, 12904.
- [16] a) Y. Xia, P. Yang, Y. Sun, Y. Wu, B. Mayers, B. Gates, Y. Yin, F. Kim, H. Yan, *Adv. Mater.* **2003**, *15*, 353; b) T. Zhai, J. Yao, *One-Dimensional Nanostructures: Principles and Applications*, Wiley, Hoboken, NJ, USA, **2012**, p. 145.